

2 Renewable Energy (RE): Bioenergy – Feedstocks and Pretreatment –

2.1 Overview

In the area of PEF-assisted microalgae downstream processing, it could be shown that parasitic microalgae precipitation is controlled by the cell's zeta potential. Appropriate adjustment of the zeta potential and the application of short pulses of several microseconds and shorter can impede unwanted biomass deposition at the electrodes of the treatment chamber.

Protocols for lipid extraction from wet microalgae biomass were optimized for recovery rates of up to 97 % of the lipid inventory. Preceding analysis of various reference methods for absolute lipid content determination revealed, that Soxhlet extraction with Hexane is the most suited method.

Investigations on basic effects of nsPEF stress responses demonstrated, that nsPEF treatment at non-lethal doses can arrest cell cycle and cause pamella states due to oxidative bursts.

Optimization of cultivation strategy reduced microalgae suspension conductivity by a factor of more than 3, which is an important step for further improving energy-efficiency of PEF-assisted microalgae processing.

Efforts to elevate PEF-processing to a new technology platform of operator-friendly semiconductor (SC) based pulsed power generators has been approached. The use of a power SC as pulse switches allows for significantly higher pulse repetition rates at moderate voltage levels at a given specific processing energy. Hence, generator size can be reduced accordingly. Currently, a 30-stage pulse generator with 30 kV rated output voltage and 600 A peak pulse current has been set up.

2.2 Control of microalgae precipitation on electrode surfaces during Pulsed Electric Field (PEF) treatment by adjustment of suspension pH

PEF treatment of microalgae has been demonstrated to exhibit processing advantages compared to conventional processing. Besides low specific energy requirements, PEF treatment can separate microalgae biomass into aqueous and oleaginous fractions. To minimize processing energy demand, the treatment of pre-concentrated microalgae suspensions is advantageous. The use of concentrated microalgae suspensions resulted in precipitation at the electrodes of cross-linear treatment chambers. Reduction of the pulse duration appeared to reduce precipitation during PEF treatment significant. Furthermore, examination of this precipitation effect revealed a correlation between precipitation behavior of different microalgae species, e.g. *Chlorella vulgaris* and *Auxenochlorella protothecoides*, and zeta potential Fig. 2.2.1. A closer inspection demonstrated that precipitation behavior of different microalgae species depends on pH of the suspension. As a result, pH-control appeared to be a suitable tool for further reduction of microalgae precipitation on electrode surfaces.

2.2.1 Zeta potential and its impact on microalgae precipitation on electrode surfaces

It is known from literature, that the zeta potential of most microalgae is negative and for that reason, we suspected that this might be a reason for predominant precipitation of algae on the anode surface. Fig. 2.2.1 displays the correlation between zeta potential and algae precipitation for two algae strains: *A. protothecoides*, and *C. vulgaris*. Both algae strains were processed with identical PEF treatment parameters (specific treatment energy, $w = 50$ kJ/kg; pulse duration, $T = 200$ μ s; electric field strength, $E = 5$ kV/cm). Fig. 2.2.1 shows that *C. vulgaris*, which exhibits a lower zeta potential in terms of absolute values, results in a smaller amount of biomass precipitated at the anode. Consequently, precipitation of *A. protothecoides* was higher.

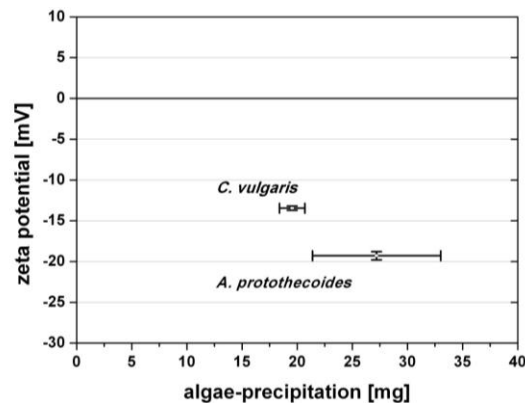


Fig. 2.2.1: Influence of the microalgae species on zeta potential and microalgae precipitation. Experiments were performed with 75 mL of algae suspension treated with 200 μ s-pulses and an electric-field magnitude of 5 kV/m. Specific energy was adjusted at 50 kJ/kg and the flow of the suspension through the treatment chamber at 0.10 mL/s. Results are mean \pm SD of two independent experiments for *C. vulgaris*, and six independent experiments for *A. protothecoides*.

2.2.2 Suspension-pH influences the zeta potential of microalgae

In order to confirm the link between zeta potential and precipitation, the zeta potential of *A. protothecoides* was modified by adjusting the pH of the suspension. Fig. 2.2.2 displays the results of a pH-titration experiment performed on *A. protothecoides* suspended in a Wu-cultivation medium. It shows the development of the zeta potential, as a function of pH, which was adjusted by addition of an increasing amount of 1 M MES (2-(*N*-morpholino)ethanesulfonic acid) solution. The results indicate that decreasing pH in *A. protothecoides* suspension induces a reduction of the absolute zeta potential value. In Fig. 2.2.2, the upper and lower limits of flocculation are shown. Within these limits, flocculation is expected and beyond these limits algae suspensions remain stable.

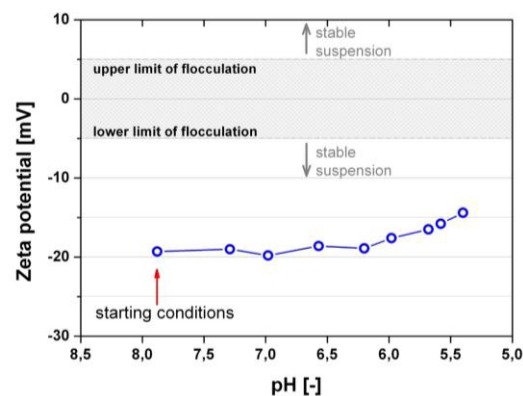


Fig. 2.2.2: Impact of pH on zeta potential of *A. protothecoides*. The pH reduction was obtained by addition of increasing quantities of 1 M MES. The upper and lower limits, where flocculation is expected are drawn.

2.2.3 Precipitation control by pH-adjustment

This result therefore supports the hypothesis that zeta potential is a major factor, influencing the quantity of microalgae that precipitates. In order to confirm the link between zeta potential and precipitation, the zeta potential of *A. protothecoides* was modified by adjusting the pH of the suspension, since the strong link between pH and zeta potential is known from the literature. To verify the impact of pH on algae precipitation by PEF processing, experiments were conducted with *A. protothecoides* either at its natural pH i.e. 7.6 or at reduced pH, i.e. 5.7. The pH-drop decreased the absolute zeta potential by 3.17 mV. Amounts of precipitated microalgae after PEF treatment ($W_{\text{spec}} = 50 \text{ kJ/kg}$, $t_{\text{imp}} = 200 \mu\text{s}$, $E = 5 \text{ kV/cm}$, $Q = 0.10 \text{ mL/s}$) are displayed in Fig. 2.2.3 for the two zeta potential values. As to be seen in the Figure, the reduction of the absolute zeta potential results in a significant reduction of microalgae precipitation on the anode surface, of 17.3 mg, i.e. by more than 50 %.

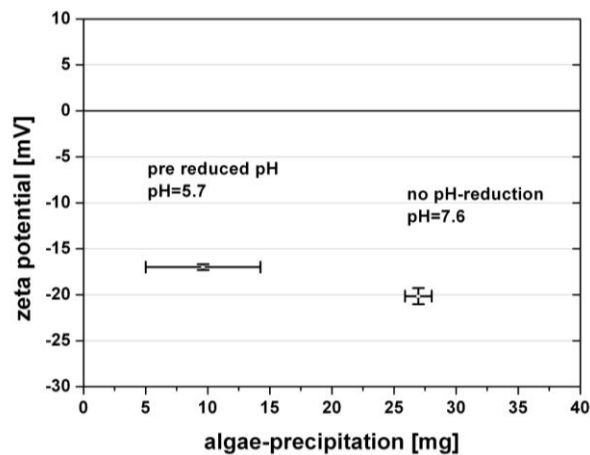


Fig. 2.2.3: Modification of zeta potential by pH reduction and consequences on microalgae precipitation. Experiments were performed with 75 mL of algae suspension (*A. protothecoides*), treated with 200 μs -pulses and an electric field magnitude of 5 kV/cm. Specific energy was adjusted at 50 kJ/kg and the flow of the suspension through the treatment chamber at 0.10 mL/s. Results are mean \pm SD of three samples in two independent experiments.

2.3 Optimization of lipid extraction from wet microalgae biomass

In previous work of the bioelectric group, it was shown that Pulsed electric field (PEF) treatment was an efficient technique to permeabilize external membranes of microalgae. This was previously demonstrated by quantification of spontaneous release of intra-cellular ions and of small carbohydrate. Additionally, it was shown that PEF pre-treatment combined with solvent extraction could greatly enhanced lipid yields. During the last year, the work program has been focused on the improvement of the lipid extraction to improve quality of solvents and to analyze the extracted oil. Focus has been set on the microalgae *Auxenochlorella prototecoides* (AP) for which our group has good expertise in the cultivation.

2.3.4 Establishment of reference methods

The first working task of this project consisted in the establishment of a reference method to analyze total lipid content of the cultivated microalgae. Three of the most popular reference methods were tested on freeze-dried microalgae: a standard method based on chloroform and methanol extraction i.e. Bligh and Dyer, a method based on methanol and methyl-tert-butyl ether (MTBE), and Soxhlet extraction using Hexane as extraction solvent.

All three methods were tested on freeze-dried microalgae, eventually additionally pre-processed with bead-milling. Results are presented on Fig. 2.3.1. From the lipid yield obtained, it appears that the Bligh and Dyer method failed to extract any lipids with or without bead-milling. Additionally, it appears that Bead-milling was necessary for efficient extraction for both Soxhlet and MTBE which is of high relevance considering that in the literature all three methods are very often used without any bead-milling. This might imply that AP microalgae are perhaps more resistant to extraction and they require an intense pre-treatment process. Based on the obtained results, Soxhlet extraction has been chosen as the reference method employed in the bioelectric group since it was more efficient with higher lipid yields and could be easily automated, leaving less room for human errors.

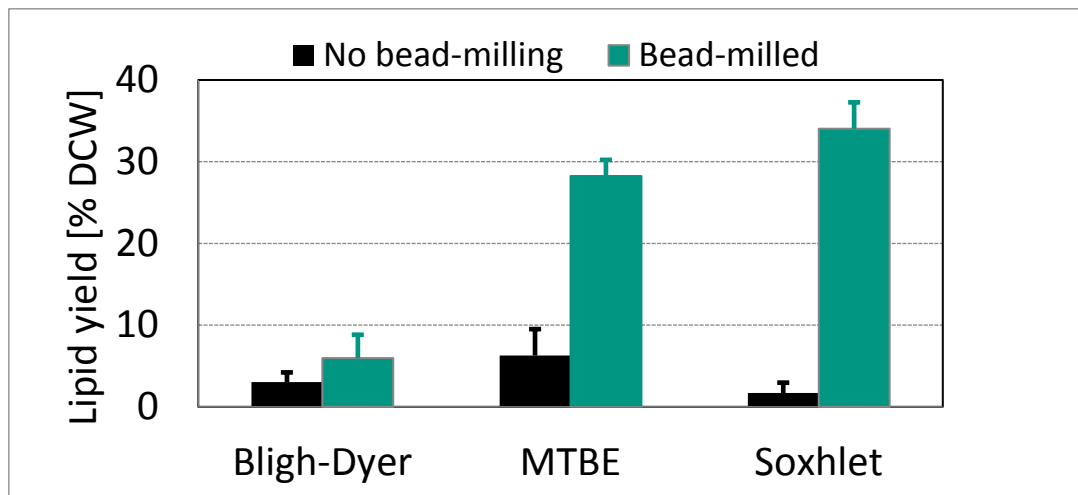


Fig. 2.3.1: Comparison of the extraction yields of three reference extraction methods: Bligh and Dyer, MTBE and Soxhlet. Extraction were performed with and without bead-milling. Blocks are the average values plus standard deviation of at least three independent extractions.

2.3.5 Extraction of lipids after PEF treatment

A standard protocol was used to process the fresh microalgae. It consisted in concentrating them at 100g/kg_{sus} by centrifugation directly after harvesting and then treating them with PEF in a continuous flow mode. Electric parameters were chosen based on previous work of our group and consisted in 1 μ s pulses with an electric field intensity at 4 MV/m applied with a repetition rate at 3 Hz. All experiments were performed with an energy input adjusted to 150 kJ per liter of suspension i.e. approximately 1.5 MJ per kg of algae dry mass.

Sham treatment consisted in submitting the sample to the flow through the treatment chamber but without any PEF treatment. After treatment, microalgae were observed under the microscope. The observation did not reveal any major change of morphology of the microalgae. The general shape and size were maintained and no debris was to be observed. In order to validate the efficiency of PEF treatment, the microalgae suspension was centrifuged after the treatment and the conductivity of the supernatant was measured. Supernatant of control samples had a conductivity of around 1.6 mS/cm at room temperature due to the ionic compounds of microalgae cultivation medium. After PEF treatment, conductivity increased by about a factor 2 and reached a value of approximately 3 mS/cm due to the release of the microalgae's intracellular ionic content. The doubling of supernatant conductivity therefore validated the efficiency of the chosen parameters for PEF treatment.

A lipid extraction protocol, inspired from Molina et. al., was adapted to be functional on wet microalgae. It is based on a hexane ethanol extraction. Results obtained with gravimetric method for different duration

of extraction are displayed on Fig. 2.3.2. The absolute lipid content of the microalgae was determined by Soxhlet and is also displayed in the Figure. The results show that the extraction procedure was inefficient for untreated microalgae and lipid yields always ranged between 1 and 4 %. PEF treatment had an outstanding effect on the extraction. The lipid yield after only one hour of extraction was on average 31 % of dry weight and therefore very close to the absolute lipid content of 37 %. The yield was further increased after 20h of extraction and reached 36 % of dry cell weight (CDW), i.e about 97% of the total lipid content.

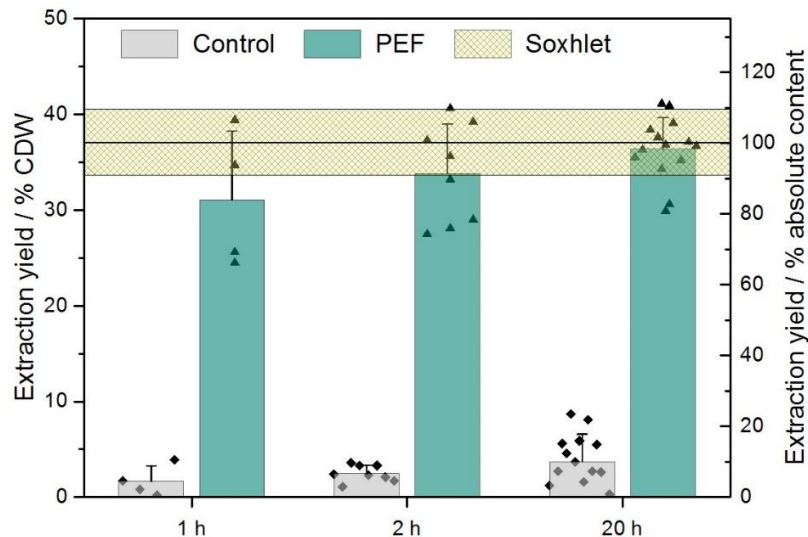


Fig. 2.3.2: Influence of PEF treatment on lipid yields obtained with solvent extraction for different extraction durations. Bars show the average plus standard deviation of at least three independent experiments. Markers show individual data points. The straight lines indicate the average plus/minus standard deviation of Soxhlet extractions. Results were obtained from mixotrophically grown microalgae *Auxenochlorella protothecoides*.

The completeness of lipid extraction could be further confirmed by using the fluorescence dye Nile-Red which stains lipids. While control samples still displayed a strong fluorescence signal indicating the presence of lipids inside the cells, the samples treated with PEF prior to extraction displayed only a very weak remaining fluorescence signal therefore confirming that the complete inventory of lipids was extracted. Currently, gas-chromatography analyses are ongoing in order to analyze the composition of the extracted oil. Preliminary analysis shows no impact of PEF-treatment on extract quality.

2.4 Nanosecond pulsed electric fields (nsPEF) trigger cell differentiation in *Chlamydomonas reinhardtii*

There are several evidences that support the basic concept of using algae as an alternative and renewable source of biomass feedstock for biofuels and/or food production. These include: high productivity per footprint, non-food based feedstock resources, use of non-arable land, reduced water demand, production of valuable co-products, etc. Due to the fast growth rate and the ability to convert light into valuable products, such as lipids, proteins and antioxidants, microalgae provide a biomass which found several applications in food, energy and pharmaceutical production. While these aspects were intensively investigated, a sustainable and economic system for algae cultivation has to be developed.

Besides the reduction of investment and operational costs of photobioreactors the increase of biomass yield, by an increased cell density or accelerated cell growth might be an alternative strategy. In previous studies, it was shown that nanosecond pulsed electric fields (nsPEF) treatment of *Arabidopsis thaliana*

seedlings and mushroom spores, results in an accelerated growth and thus to an increased yield of fruit bodies, in case of mushrooms. Nevertheless, in the efforts to stimulate algal growth by means of nsPEF treatment these effects were contradictory. In order to clarify this contradiction, basic investigations on signaling pathways for nsPEF induced stress reactions of microalgae have been study in the frame of a doctoral thesis. In general, plants, including microalgae, perceive environmental signals (abiotic and biotic stress) and further them to cellular machinery to activate adaptive responses.

In this study the unicellular green algae *Chlamydomonas reinhardtii* was used as experimental model to analyze the cellular responses evoked by nsPEFs. It could be observed that nsPEFs induce a short-term permeabilization of the membrane, accompanied by swelling and oxidative bursts. Furthermore, these responses were enhanced when the pulse duration increased from 25 ns to 50 ns. These responses are transient, but are followed, several days later, by a second wave of oxidative bursts, arrested cell division, stimulated cell expansion and the formation of an immobile palmella stage, Fig. 2.4.1. Both the stimulation of cell expansion and the formation of palmella stages, correlate with a persistent long-term increasing of lipid peroxidation. While the spontaneous formation of palmella stages could be suppressed by exogenous indol acetic acid (IAA), the palmella formation in response to nsPEFs was not responsive to exogenous auxin. Our data show that nsPEFs release a long-lasting signal that persists, although the immediate cellular changes to the treatment are mostly reversed in the first two hours after pulsing.

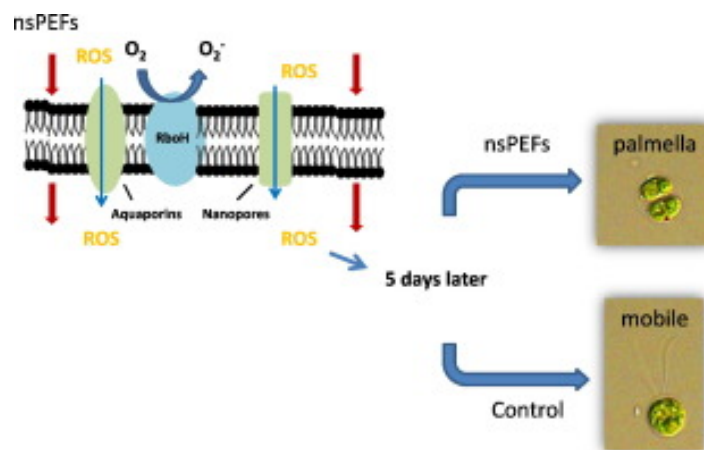


Fig. 2.4.1: Induction of palmella stage in response to pulse treatment. Representative cells after nsPEFs treatment. [Bai et al. BBA Biomembranes 2017, 5:1859].

The highlights of this study are:

- nsPEFs induce rapid membrane permeability, volume increase and lipid peroxidation,
- Cell responses to nsPEFs enhanced when pulse duration increased from 25 ns to 50 ns,
- Cell cycle arrested and palmella stages appeared during long-term response to nsPEFs,
- nsPEFs induced irreversible palmella stages could not be suppressed by exogenous IAA.

2.5 Bacterial decontamination of industrial water and paints by means of pulsed electric fields (DiWaL –Project)

In the framework of three-year project, focus on the “Decontamination of Industrial Water and Paints” DiWaL, a consortium of research institutions and manufacturers, under the coordination of KIT, has started the work on November 2016. DiWaL is funded by the Federal Ministry of Education and Research (BMBF), and has a total budget of 2.9 million euros. The main objective of the project DiWaL, is to develop innovative water-management solutions and enhanced designs for pretreatment and electrocoating systems, by employing the PEF technology, in order to improve the efficiency and the sustainability. The aim of this concept is to prevent the bacterial contamination in the pretreatment and coating process in order to eliminate the use of biocides and to reduce both fresh water consumption and waste water generation.

DiWaL bundles the experiences of partners from research, Karlsruhe Institute of Technology (KIT) and Pforzheim University of Applied Sciences, as well as production-system specialist Eisenmann SE, paint manufacturers Emil Frei and PPG Deutschland, PPG Deutschland Business Support GmbH and carmaker BMW Group. The joint project to improve decontamination of industrial water and paints commenced on November 1, 2016 and will conclude on October 31, 2019.

2.6 Microalgae cultivation for low suspension conductivity during biomass harvest

The energy demand for PEF treatment in microalgae downstream processing scales with the conductivity of the suspension to be processed. In order to avoid additional energy-extensive washing steps, a low conductivity value of the microalgae suspension of 1 mS/cm and lower at the end of the cultivation is desired. Recent values achieved at the outdoor photobioreactor ranged between 3 mS/cm and 4 mS/cm, when operated without conductivity-optimized control algorithms.

In 2016 headed by BVT cultivation media and conditions were optimized on lab-scale for low-conductivity at the end of the cultivation.

Based on ICP-OES analyses the medium components were adjusted according to the elemental composition of *Chlorella vulgaris* for a final cell dry weight of 5 g/L.

In previous outdoor cultivations the pH was adjusted by NaOH titration until the medium was saturated with CO₂. Due to Na⁺-ions of the titration solution and a medium composition which was not tailored to the needs of the algae the conductivity of the suspension unnecessarily increased.

Cultivation with optimized control parameters and medium was carried out in a 1.7 L stirred tank reactor with continuous illumination. After cultivation time of approx. 140 h a cell dry weight of 5 g/L at a conductivity of less than 1 mS/cm was achieved. In the upcoming year this approach will be implemented and tested for feasibility at the outdoor flat panel photobioreactor “pbr1000”.

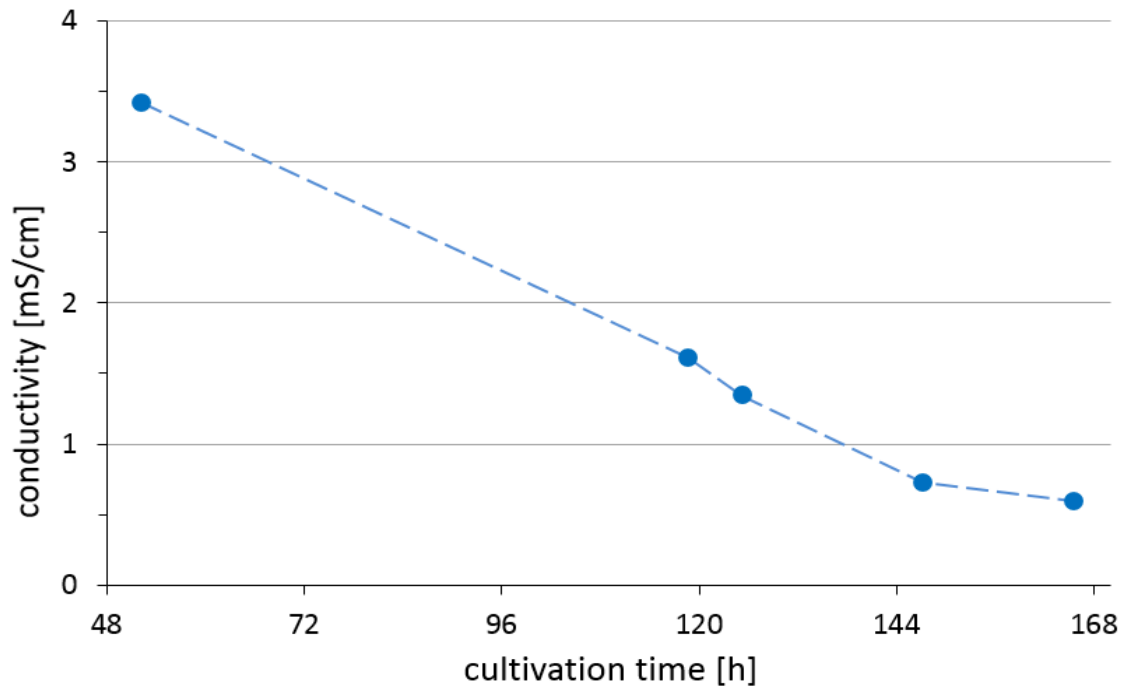


Fig. 2.6.1: Change of suspension conductivity during a batch cultivation of *C. vulgaris* in a stirred tank reactor with optimized medium composition and improved control algorithms.

2.7 Electroporation of crushed grapes and development of semiconductor based generators

In cooperation with the University of Otago, New Zealand, the electroporation device KEA-WEIN has been operated on-site in a winery in New Zealand in March and April 2016. Approximately 2 t of Merlot grapes have been processed successfully. The goal of the trials was to combine electroporation with the method of fermentation on skins, which is the common processing method for grapes of red grape varieties in New Zealand. Chemical and sensorial analysis of must and wine has been performed by Prof. Oey and her colleagues from the University of Otago.



Fig. 2.7.1: Electroporation device KEA-WEIN on site in a winery in autumn 2016.



Supported by:



Federal Ministry
for Economic Affairs
and Energy

on the basis of a decision
by the German Bundestag

In the frame of a joint cooperation between ARMBRUSTER Keltertechnologie, KEA-TEC, the State Institute for Viticulture and Enology, Freiburg, and KIT/IHM the technology of the electroporation of crushed grapes is currently transferred to industrial partners. This work is supported by the Federal Ministry for Economic Affairs and Energy on the basis of a decision by the German Bundestag. For the experiments in autumn 2016 the electroporation device KEA-WEIN has been upgraded to a flowrate of 2 t/h. Fig. 2.7.1 shows the electroporation device set up in a winery. The increase in flow rate has been achieved by combining a scale-up of the electroporation reactor with an increase in flow velocity. Scaling allows for an easy adaptation in size of an already existing design for an electroporation reactor without the need for field calculations. The electrode distance has been increased from originally 35 mm to 44 mm, which corresponds to an increase in tube diameter from DN40 to DN50. In combination with the existing Marx generator and power supply the new design allows for a peak electric field strength inside the electroporation reactor of $\hat{E} = 44 \text{ kV/cm}$ and a strongly damped periodic pulse shape. For a higher flow rate of crushed grapes the pulse repetition rate of the Marx generator has been increased by implementing a nozzle for each spark gap switch. The nozzles guide the flow of nitrogen gas inside the spark gap housing directly to the gaps between the electrodes and hence provide a fast removal of debris. At a charging voltage per stage of 50 kV a pulse repetition rate of 39 Hz has been achieved. Fig. 9 shows the charging voltage per stage. As the power supply uses a control scheme based on pulse packets, the voltage increases stepwise. During the experiments in autumn 2016 in a winery crushed grapes of four different grape varieties (Riesling, Mueller-Thurgau, pinot noir and Zweigelt) have been processed successfully. The wine is currently processed.

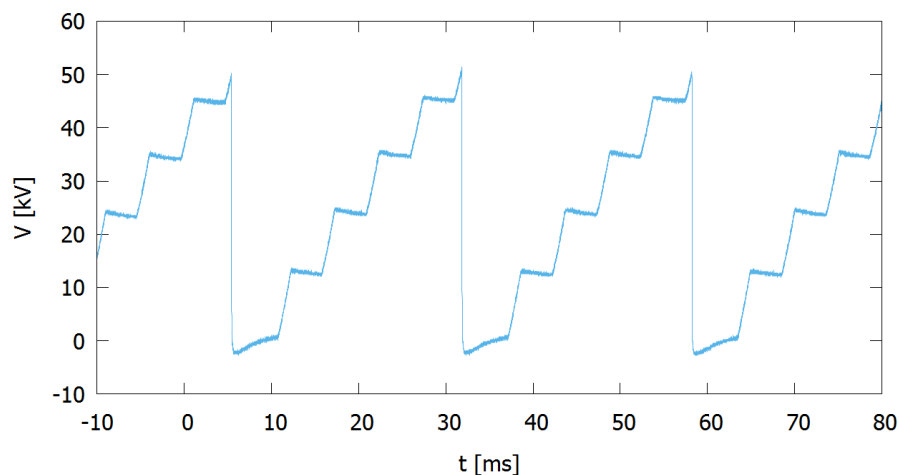


Fig. 2.7.2: Charging voltage of one stage of the Marx generator.

For the use in a PEF treatment device pulse circuits based on a series connection of capacitor, inductance, and the resistance of a PEF treatment reactor (RLC circuit) are well established for large-scale devices equipped with spark gap switches. However, the combination of such a RLC-based pulse circuit with a semiconductor-equipped Marx generator enables energy-efficient soft switching of the semiconductor switches. In last year's annual report a ten-stage Marx generator according to this design concept has already been presented. Now, a 30-stage Marx generator with IGBT switches has been developed and tested successfully. For the tests the stages have been arranged in three stacks of ten stages each (Fig. 2.7.3).



Fig. 2.7.3: Pulse generator comprising 30 modules.

The generator has been designed for a stage voltage of 1 kV. The charging path comprises current-compensated charging coils allowing for a simple single-switch design of each stage and low voltage drop during charging. The pulse generator has been tested in a circuit with an inductance $L = 70 \mu\text{H}$ and a load resistance of $R = 37.5 \Omega$. Fig. 2.7.4 shows the voltages measured at the outputs of stages #10, #20, and #30 together with the current through the load resistance. The fast voltage rise in combination with the rather slow rise of the current demonstrates the zero-current switching condition during switch-on. The switches open after complete discharge of the capacitors. In case of a flash-over at the load shorting the electrode system of the electroporation reactor immediate opening of the switches is desired to limit the energy fed into the ark. However, when opening the switches during pulse application the circuit inductance continues to drive a current. To enable a fast decay of the current the stages have been equipped with a circuitry for active voltage clamping instead of using bypass diodes. Fig. 2.7.5 shows the voltages at each stage and the load current for a three-stage configuration during active clamping. Equal voltage distribution between the stages has been achieved both during pulse application and voltage clamping. Under clamping conditions the current decays nearly linearly down to zero. The energy is transferred partly back into the stage capacitors and partly dissipates into heat at the IGBT switches.

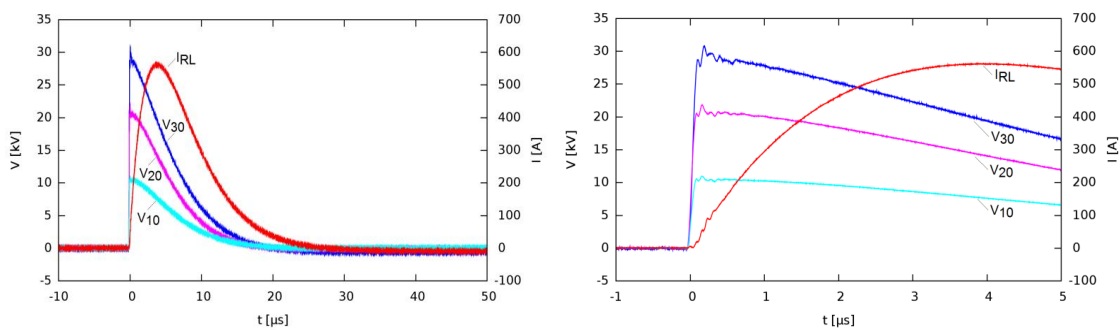


Fig. 2.7.4: Test of 30-stage generator at 1 kV per stage ($L = 70 \mu\text{H}$, $R_L = 37.5 \Omega$): Voltage at stages 10, 20, and 30 (V_{10} , V_{20} , V_{30}), and current through load (I_{RL}): left: whole pulse, and right: voltage- and current rise.

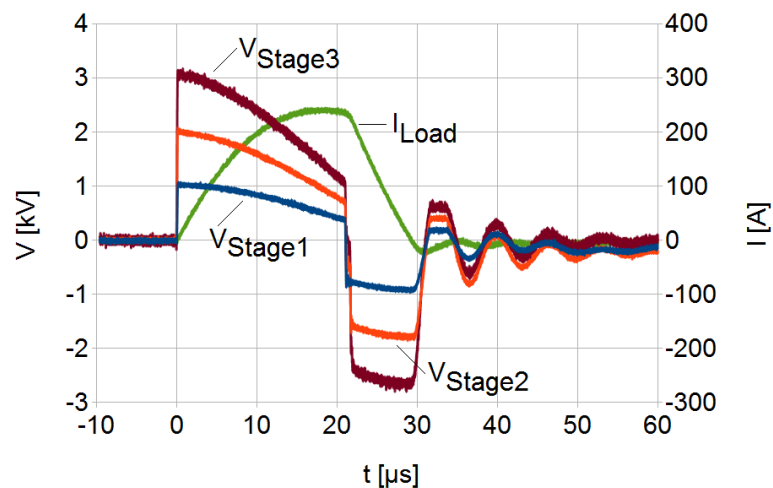


Fig. 2.7.5: Active clamping in a 3-stage configuration: Equal voltage distribution between stages.

Involved Staff:

K. Baumann, H. Brüsemeister, J. Fleig, **Dr. W. Frey**, Dr. C. Gusbeth, D. Herzog, M. Hochberg, S. Keipert, K. Leber, Prof. G. Müller, K. Paulus, D. Quattrocchi, **Dr. habil. M. Sack**, Frau Dr. A. Silve, DI R. Sträßner, R. Wüstner

2.8 Concentrating solar power (CSP)/ Liquid metal – Material research – improving the compatibility of materials for CSP

The use of liquid metals as heat-transfer- and storage media for CSP is a new research area started in the frame of POF3 together with IKET, INR and IAM. The basis of this work including experimental capabilities is funded on the experience and expertise gained in the last years on research performed in the nuclear program. Based on fundamental aspects of material liquid metal compatibility material concepts and related experimental are the major target of our research. Surface modification of materials using pulsed electron beams is well established in the nuclear community dealing with the use of liquid metal coolants. In-situ diagnostics of beam formation and target beam interaction will be targeted combining a new constructed GESA – SOFIE and simulations using MAGIC and other software tools. In addition to Na, Pb, Pb-alloys and Sn are investigated as possible CSP heat transfer materials. In the past extensive investigations regarding material compatibility with these liquid metals (especially with Pb and Pb-alloys) were done, but mainly below 550°C. The available corrosion test facilities (COSTA) for Pb, Pb alloys and Sn ca be operated also at temperatures above 600°C, which is the temperature range required for being used in CSP devices.

2.8.1 Development of material concepts for the use of liquid metals at high temperatures

Design and construction of Na corrosion test facilities for CSP tower receivers

The most promising liquid metal to be employed as heat transfer media in CSP tower receivers is liquid Na. Na was already used in the past for this purpose, but some Na fire stopped all activities in that direction. Therefore, all materials that are intended to be used have to be fully compatible with Na and no stress induced failure is allowed. Most steels are corrosion resistant at least up to 650°C in oxygen free Na. For

efficient use of CSP the final target is to operate the receiver at temperatures above 750°C. To assure the use of steels and Ni-based alloys and surface modified materials corrosion test in stagnant Na are envisaged. The day and night cycle and the occurrence of clouds induce stresses in the materials. Rapid temperature changes at high temperatures will be simulated by a dedicated test facility. Two temperature ranges are considered to be of interest. For short term realization of Na as CSP heat transfer media HT-steels without and with surface engineering (alloying with non-soluble materials or Al including pre-oxidation) will be tested at temperatures below 700°C. For long term perspective higher temperatures up to T_{boil} of 883°C are the target. There Ni base alloys with and without surface engineering, Ceramics, Maxphases or new concepts like WCu-laminated tubes will be considered.

Compared to experiments performed with Pb alloys in the past Na requires significant improved safety measures that assure to avoid any contact of Na at high temperatures with water and air. Therefore, a new Na-Corrosion lab containing a COSTA-SOL for corrosion tests in stagnant Na at temperatures up to 880°C and a high temperature thermal cycling loop SOLTEC-TCT (700°C + 880°C) was established.

The COSTA facility COSTA-SOL for Na was build, attached to the glovebox and taken into operation. The Na-melting pot was installed in the glovebox and first Na handling efforts were performed (Fig. 2.8.1). Oxygen and moisture content in the glovebox are still too high for handling oxygen free sodium. Therefore, an oxygen and moisture control loop is designed and will be attached to the glovebox. Anyway, to reduce further the oxygen and moisture content in the glovebox an additional heated stainless steel pot containing Na or Li at elevated temperature will be placed in the glovebox. This open liquid metal will be used to reduce the remaining oxygen and moisture before handling the Na. In a first test at 600°C Na was filled in an alumina crucible and placed inside the stainless steel tube of the furnace. To reduce the oxygen content of the Ar+5%H₂ gas that is purged during the exposure experiment even more, the gas passes an additional furnace at around 650°C via a steel tube filled with Zr metal wire.

The design of the high temperature thermal cycling loop SOLTEC-TCT consisting of two parts, the loop and the thermal cycling test (TCT) section was already described. The SOLTEC-TCT, whose final design is shown in Fig. 2.8.2, is under construction, finally. The TCT section is ready to be adapted to the loop.



Fig. 2.8.1: Na heating and filling pot located in glovebox.

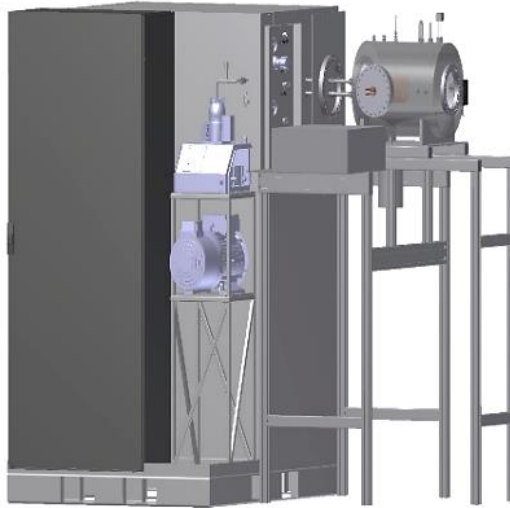


Fig. 2.8.2: Sketch of SOLTEC-TCT loop and thermal cycling test section.

High temperature compatibility test of steels and commercial FeCrAl materials in Pb

Beside Na, Pb is still an option as heat transfer fluid in. The SOMMER (Solar furnace with Molten Metal REceiver) facility, designed and build by our colleagues from IKET, will use Pb as heat transfer media with a maximum temperature of about 650 °C. The first version of the receiver will be built from stainless steel. To explore possible construction materials exposure tests performed some time ago with two steels, 1.5471 and alloy 800, and alumina containing Fe-base alloys from Kanthal performed at 600 and 750 °C in Pb with an oxygen content of 10^{-6} and 10^{-8} wt% for a duration of 1000 h were re-evaluated. The steel 1.4571 do not exhibit any corrosion attack at 600 °C, while the alloy 800 exhibit dissolution corrosion at the lower oxygen conditions. All tested Kanthal alloys show excellent behaviour even at 750°C in Pb with 10^{-6} wt% oxygen. Thin Al_2O_3 scales develop at the surface and protect the materials. The alloy 800 shows locally dissolution attack that alter with Cr enrichment at the surface accompanied by deep internal oxidation. The austenitic steel 1.4571 forms a Fe rich outer Fe-Cr scale with an internal oxidation zone of about 100 μ m. Some Pb penetrated the Fe-Cr scale but not resulting in sever dissolution attack, at least after 1000 h of exposure. At 750 °C in Pb with low oxygen (10^{-8} wt%) however, only one FeCrAl-alloy survived (Fig. 2.8.3), the Kanthal Akrothal with 15Cr and 4 wt% Al. A thin almost non visible oxide scale prevents the dissolution attack. All other Kanthal alloys with higher Cr content as well as the two steels (alloy 800, 1.4571) showed severe dissolution attack (Fig. 2.8.3).

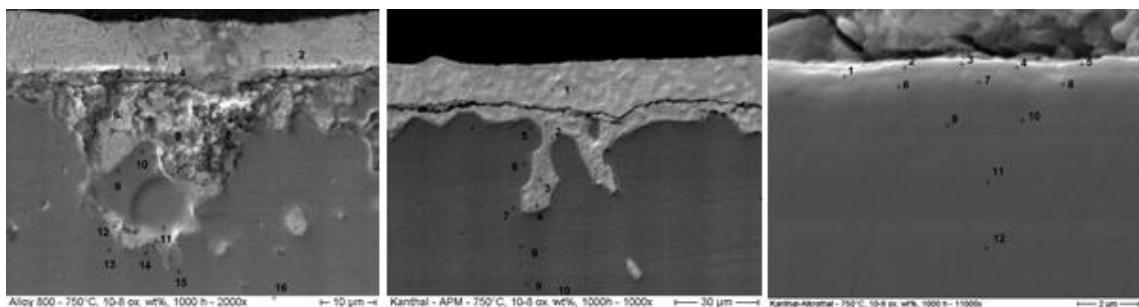


Fig. 2.8.3: SEM of cross sections of (from left to right) alloy 800, Kanthal APM and Kanthal Akrothal after 1000h exposure to Pb at 750°C with 10^{-8} wt% oxygen.

Whether the Kanthal Akrothal as the best behaving of these materials can be employed for use in CSP even at 750°C with Pb as heat transfer media requires longer exposure tests at similar conditions. However, for

SOMMER, the Pb cooled KIT CSP Demonstrator, both steels and all the Kanthal alloys can be used at least for short term operation of 1000 h.

Alumina-forming high entropy alloys

High-entropy alloys constitute currently an important scientific topic for materials researchers and engineers due to their unique and even intriguing compositions, microstructures and engineering properties, such as high strength and toughness, creep and corrosion resistance.

Containing five or more principal elements (concentrations of each element ranging from 5 to 35 at. %), in contrast with the conventional metallurgical alloy-design, they form disordered solid solutions with face-centered cubic, body-centered cubic or hexagonal closed-pack structures. Thus, HEA concept with a vast number of elemental combinations, offers the possibility to design technologically relevant alloys, containing stable oxide-former elements and refractory elements, with an immense potential for high temperature applications. Recent studies on high-entropy alloys reporting good phase stability following ion irradiation up to 50 dpa make them potential candidates for the structural materials in fusion and fission reactors. Therefore, the possibility to produce HEAs with a combination of high corrosion, high creep and high irradiation resistances properties, which are required for structural materials in energy-related high temperature applications, must be explored.

It is known that molten lead and lead alloys are under consideration as working fluids for various energy-related applications, such as advanced nuclear reactors and concentrated solar power. However, the compatibility of such environment with structural steels, in terms of corrosion and mechanical resistance, causes considerable concerns.

We report some preliminary results on the corrosion behaviour of aluminium containing high-entropy alloys exposed to oxygen containing molten lead at 600°C.

Five alloys belonging to the AlCrFeNiX (X: Co Mn) high-entropy alloy system, with small addition of reactive elements (Y, Zr), were synthesized from high purity elements using arc melting procedure.

Prior to corrosion testing, the microstructure of the alloys was evaluated using scanning electron microscopy combined with energy dispersive X-Ray spectroscopy (SEM/EDS) methods. Backscattered electron images (BEI) of the as-cast alloys revealed that the microstructure consists of large, columnar grains with dendritic sub-structure (Fig. 2.8.4).

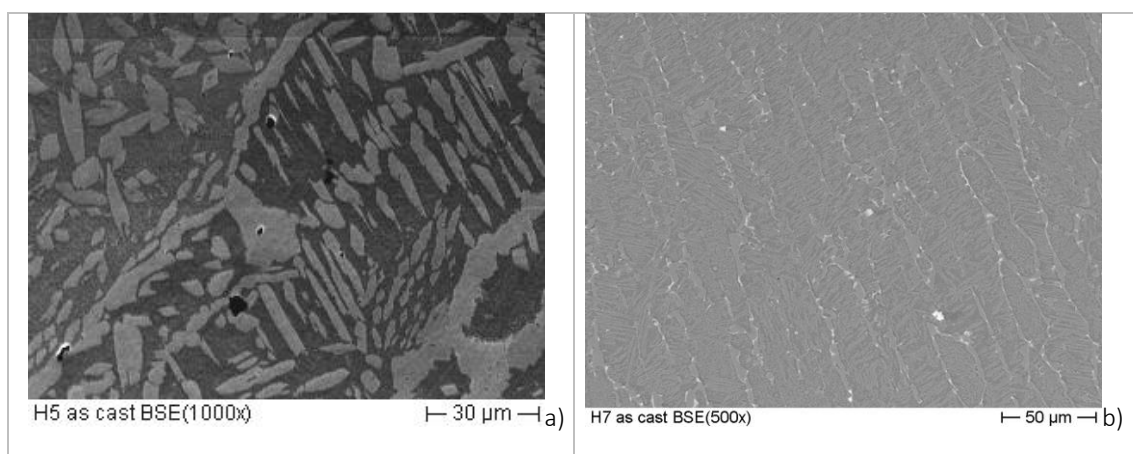


Fig. 2.8.4: Backscattered electron images (BEI) of the $\text{Al}_{11.1}\text{Cr}_{22.2}\text{Fe}_{22.2}\text{Ni}_{22.3}\text{Mn}_{22.2}$ (a) and $\text{Al}_{12.7}\text{Cr}_{21.6}\text{Fe}_{21.7}\text{Ni}_{21.7}\text{Co}_{21.6}\text{Zr}_{0.7}$ (b).

The phase composition of the alloys was determined using X-Ray diffraction (XRD). The phases constituting the as-cast alloys are the f.c.c and b.c.c., as can be seen in the patterns presented in Fig. 2.8.5.

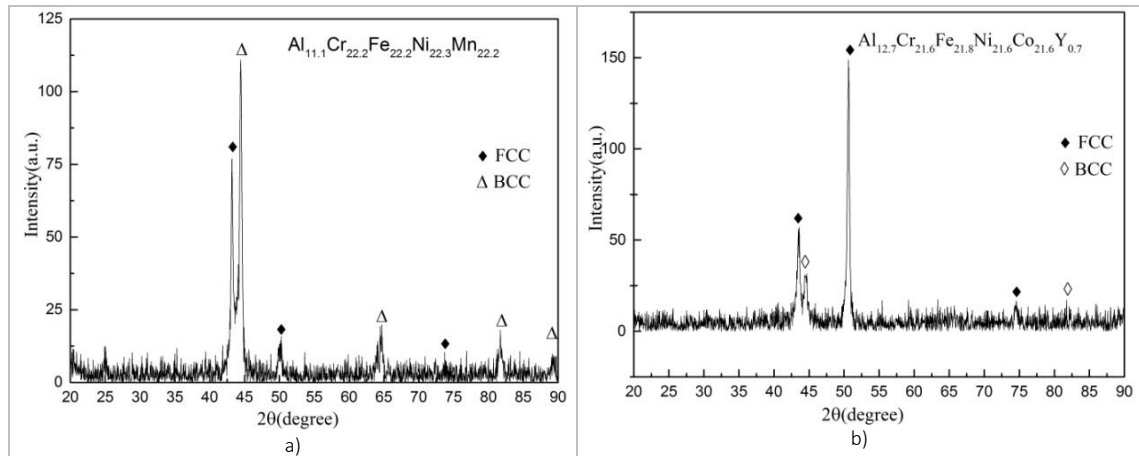


Fig. 2.8.5: XRD patterns of $\text{Al}_{11.1}\text{Cr}_{22.2}\text{Fe}_{22.2}\text{Ni}_{22.3}\text{Mn}_{22.2}$ (a) and $\text{Al}_{12.7}\text{Cr}_{21.6}\text{Fe}_{21.8}\text{Ni}_{21.6}\text{Co}_{21.6}\text{Y}_{0.7}$ (b) alloys in as-cast state.

The alloys ingots were cut into discs with around 1.2 mm thickness. All specimens were mechanically grinded with 1200 grit abrasive SiC paper and then were exposed to stagnant molten lead containing 10^{-6} wt.% oxygen in COSTA facility, at 600°C for 3500 hours. After the extraction from the melt the specimens were cleaned with a solution of ethanol, acetic acid and hydrogen peroxide (1:1:1) to remove the remaining adherent lead and to make the oxide layer itself accessible for inspection.

The morphology of the oxide scales grown, during the exposure to oxygen-containing molten lead, on the surface of the specimens was examined by SEM. No dissolution attack was observed for any of the samples tested. The general aspect is generally smooth as can be observed in Fig. 2.8.6.

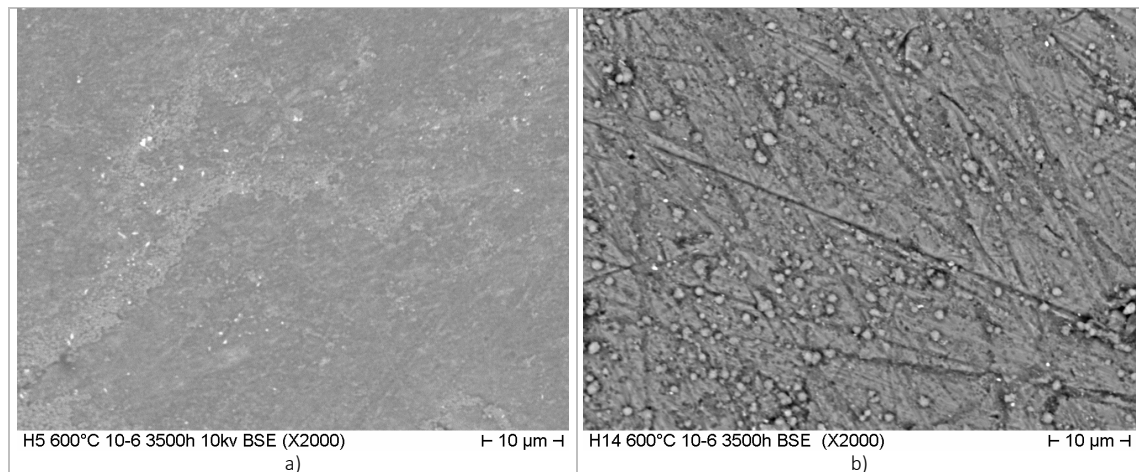


Fig. 2.8.6: Examples of the morphologies of the oxide scales grown, during the exposure to oxygen containing molten lead, on the surface of the specimens made from alloys $\text{Al}_{11.1}\text{Cr}_{22.2}\text{Fe}_{22.2}\text{Ni}_{22.3}\text{Mn}_{22.2}$ (a) and $\text{Al}_{13}\text{Cr}_{21.7}\text{Fe}_{21.8}\text{Ni}_{21.8}\text{Co}_{21.7}$ (b).

The cross section examination of the specimens revealed that the samples are covered by a protective oxide scale with thickness varying from around $2\ \mu\text{m}$ in case of the alloy $\text{Al}_{11.1}\text{Cr}_{22.2}\text{Fe}_{22.2}\text{Ni}_{22.3}\text{Mn}_{22.2}$ to less than $0.5\ \mu\text{m}$ in case of the samples made from $\text{Al}_{13}\text{Cr}_{21.7}\text{Fe}_{21.8}\text{Ni}_{21.8}\text{Co}_{21.7}$ and $\text{Al}_{12.7}\text{Cr}_{21.6}\text{Fe}_{21.7}\text{Ni}_{21.7}\text{Co}_{21.6}\text{Zr}_{0.7}$ alloys (Fig. 2.8.7).

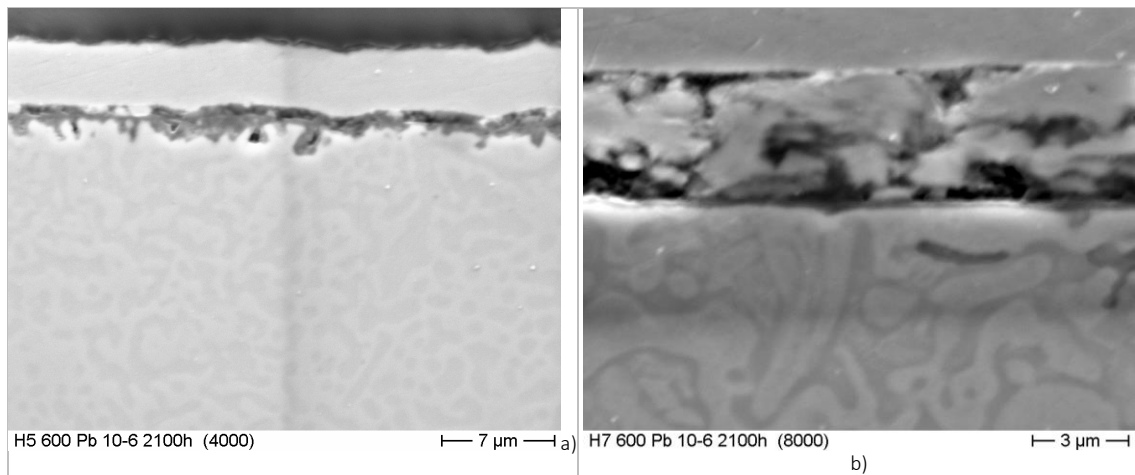


Fig. 2.8.7: Cross sections of the samples made from $\text{Al}_{11.1}\text{Cr}_{22.2}\text{Fe}_{22.2}\text{Ni}_{22.3}\text{Mn}_{22.2}$ (a) and $\text{Al}_{12.7}\text{Cr}_{21.6}\text{Fe}_{21.7}\text{Ni}_{21.7}\text{Co}_{21.6}\text{Zr}_{0.7}$ (b) alloys exposed to oxygen containing molten lead for 3500h at 600°C. The scale thickness varies from around 2 μm (a) to less than 0.5 μm (b).

The line scan presented in Fig. 2.8.8 (a), shows a duplex oxide scale which protect the sample made from $\text{Al}_{11.1}\text{Cr}_{22.2}\text{Fe}_{22.2}\text{Ni}_{22.3}\text{Mn}_{22.2}$ against dissolution attack. The outer layer is an Al-rich oxide, while the inner layer is an oxide rich in Mn. In case of the sample made from $\text{Al}_{13}\text{Cr}_{21.7}\text{Fe}_{21.8}\text{Ni}_{21.8}\text{Co}_{21.7}$ the protective layer grown only below the initial sample surface and is rich in Al (Fig. 2.8.8 b)

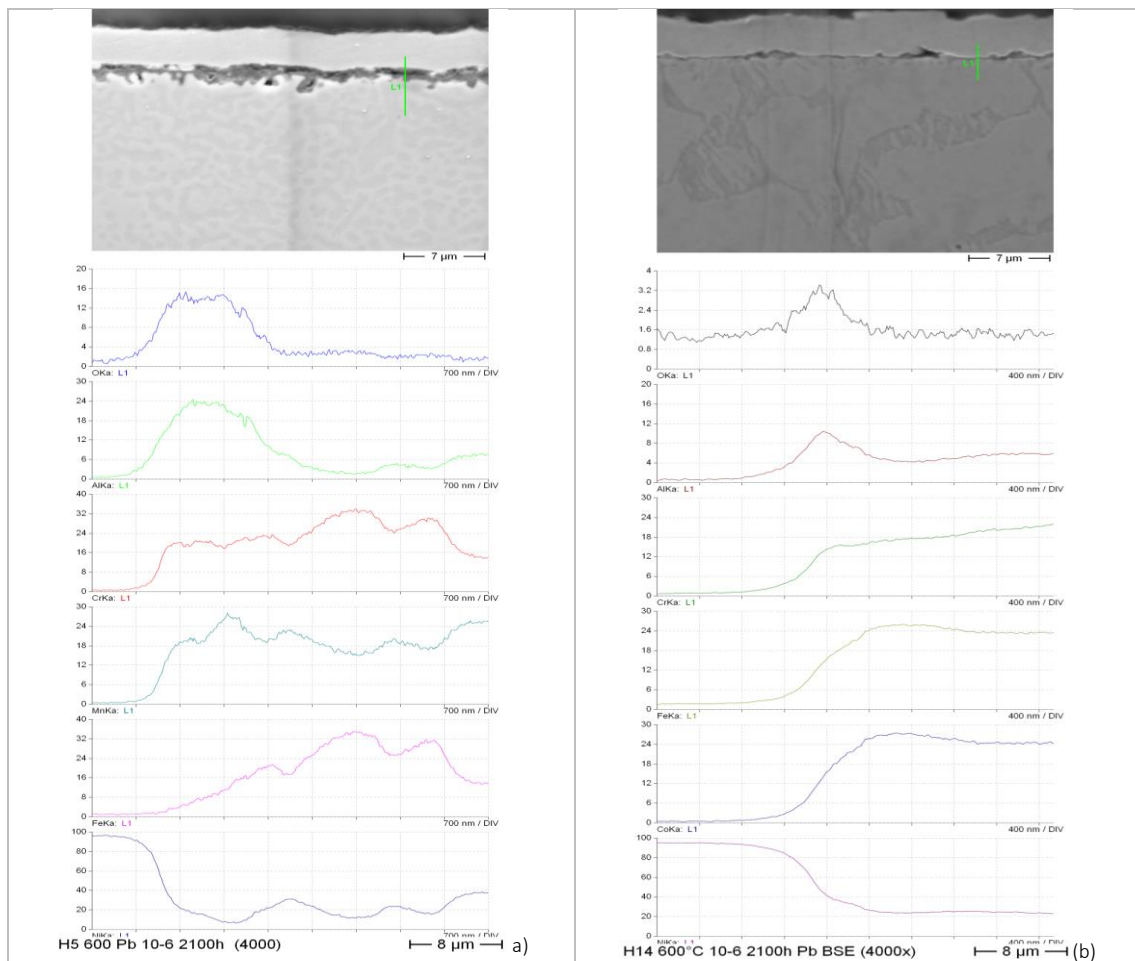


Fig. 2.8.8: EDX line scan showing the duplex oxide scale formed on $\text{Al}_{11.1}\text{Cr}_{22.2}\text{Fe}_{22.2}\text{Ni}_{22.3}\text{Mn}_{22.2}$ sample (a) and the EDX line scan of a very thin Al-rich oxide scale formed on $\text{Al}_{13}\text{Cr}_{21.7}\text{Fe}_{21.8}\text{Ni}_{21.8}\text{Co}_{21.7}$ sample.

The research program covering the high-entropy alloys for energy related applications will be continued during next period with activities concerning HEA's structural stability at high temperatures and under irradiation, corrosion resistance and mechanical properties. Exposure test in Pb at even higher temperatures and in Na will follow.

2.8.2 GESA-SOFIE and related simulations

The quasi-planar GESA consists of three functional regions: beam formation; beam compression and transport; target. The regions can be characterized concerning their influence on the beam quality. At the target an ion beam is formed, which has moderate influence on the electron beam; in the compression and transport region, the electron energy and beam diameter are limited from below; the beam formation region has a strong influence on the beam stability and the limitation of the beam intensity and pulse duration. Therefore, the region of beam formation is essential regarding the fundamental applicability of the electron beam for surface treatment and the investigations of GESA-SOFIE focused on the cathode-grid gap and beam formation.

In order to minimize the influence of the other functional regions (compression and transport, target) on the processes in the cathode-grid gap, a few measures were taken:

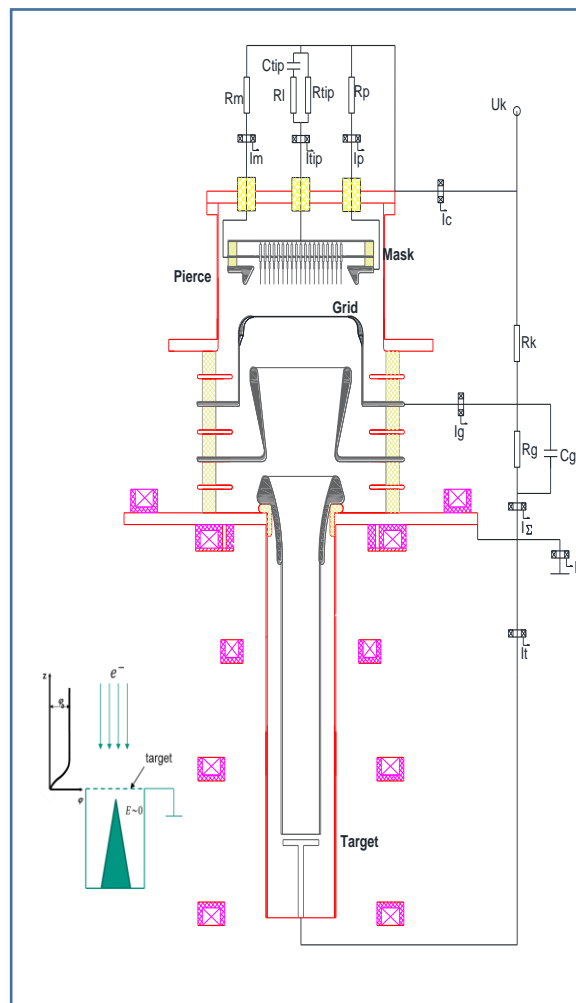


Fig. 2.8.9: Circuit of GESA-SOFIE. Position of current measurements.

Target built in the shape of a Faraday cage with 90% transparency of the entrance grid. Target plasma is formed inside the cage where only weak fields exist. Thus, the ion flow towards the cathode is suppressed. Additionally, the collector is cone-shaped with opening angle 15° at the tip in order to reduce the energy density at the target.

Installation of additional electrodes and change of transport channel diameter. The beam potential between grid and target becomes monotonic, thus trapping of electrons is avoided.

Reduction of magnetic field in transport channel. The beam diameter at the target is increased and thus deposited energy density is further reduced.

All GESA facilities are equipped with cathodes based on multipoint explosive emission. The emission plasma is generated at the tips of carbon fiber bundles. The fiber bundles are connected via resistors (1 – 2 kOhm), which limit the currents to the fibers until all tips are ignited ($\sim 100\text{ns}$). The general observation of GESA operation with default parameters is an increasing perveance during the pulse. This increase cannot be completely captured by the voltage change. It can be concluded that the effective distance of the acceleration gap continuously decreases with time. Possible causes are the motion of the emission front towards the grid and/or generation of plasma at the grid.

Our investigations aim at

1. Motion of the cathode plasma front – origin and possibility of control;
2. Grid plasma – formation and influence on gap impedance.

The cathode region was reconstructed to allow current and voltage measurements on each component in contact with the cathode plasma. The components are connected to the circuit outside the vacuum chamber. This allowed flexible adjustment of the voltage distribution between the components and thus indirect control of the cathode plasma parameters.

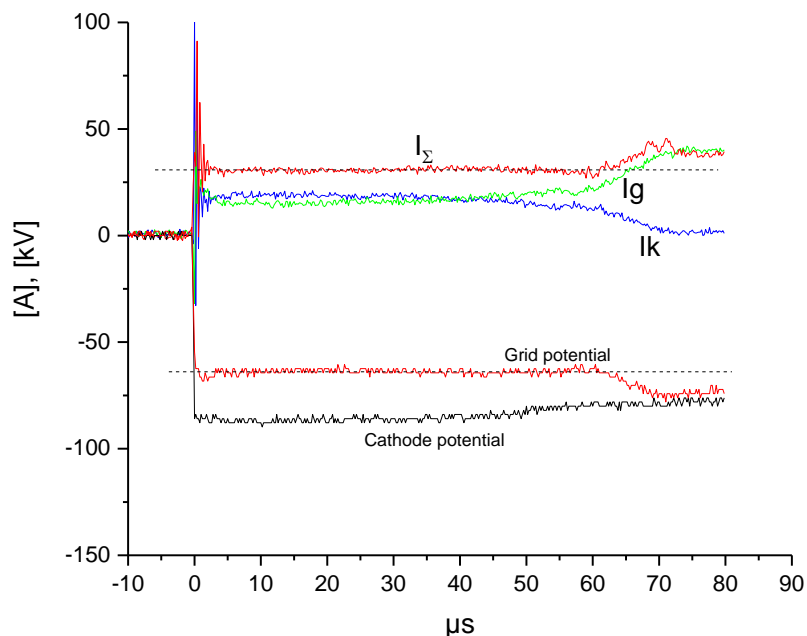


Fig. 2.8.10: Grid potential is independent of grid current.

The grid potential is adjusted by the choice of the resistances R_k and R_g (Fig. 2.8.9). In order to minimize the influence of grid current variations on the emission plasma behavior, a constant grid potential is intended. This is feasible if R_k is chosen as small as possible compared to R_g . For constant cathode potential we have

$$dI_k = -\frac{R_g}{R_k + R_g} dI_g$$

Thus, for $R_k \ll R_g$ the change of the grid current, dI_g , is compensated by the change of dI_k and the sum that controls the grid potential is constant, $I_\Sigma = I_k + I_g$ (Fig. 2.8.10).

The streak camera Hamamatsu C7700 was used to observe the dynamics of cathode and grid plasmas. The imaging system is telecentric both on the objective and on the image side so that the cathode-grid gap is imaged with minimum perspective deformation. The framing camera Memrecam HX-3 (NAC Image Technology) was used to monitor spatial distribution and ignition behavior simultaneously at cathode and grid.

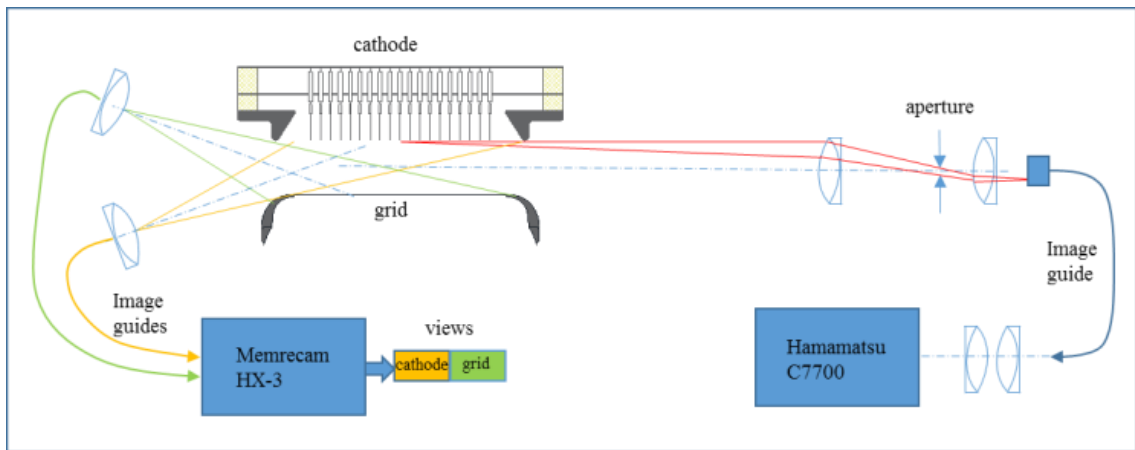


Fig. 2.8.11: Setup for optical diagnostics.

Results: Cathode plasma

Current and voltage waveforms as well as streak images of a typical GESA-SOFIE pulse are shown in Fig. 2.8.12. The currents on the Pierce electrode and on the mask start immediately after the onset of the pulse and their qualitative evolution is identical to the one of the emission current, I_c . In spite of the significant distance of mask (50 mm) and Pierce electrode (30 mm) to the carbon fiber tips, the signals start without detectable time delay. Because the plasma expansion towards the mask occurs in a region of weak electric field, the expansion velocity can reach tens of $\text{cm}/\mu\text{s}$.

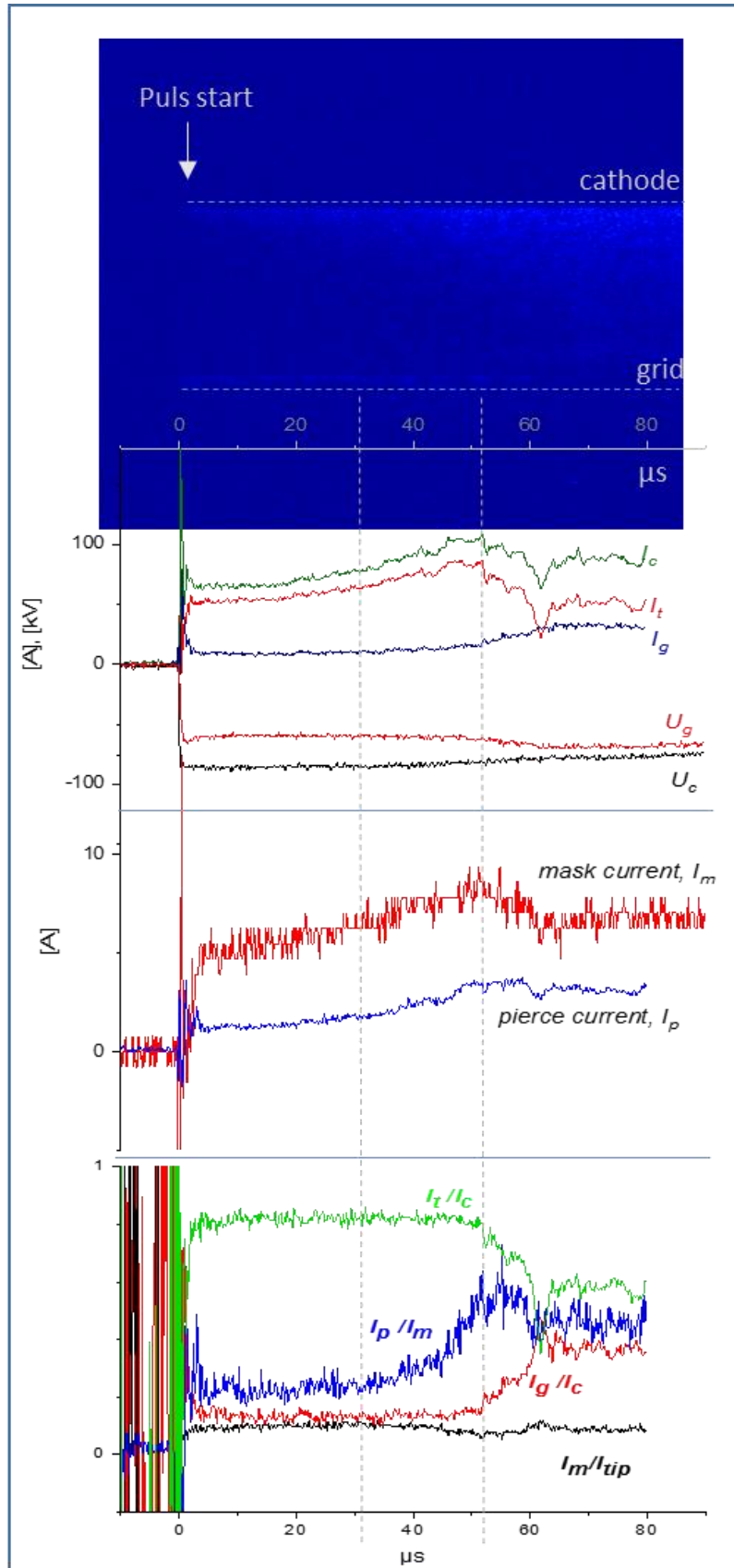


Fig. 2.8.12: Typical current and voltage waveforms of GESA-SOFIE.

In general, the currents on the mask and Pierce electrode can be composed of three contributions: ion current from grid and target plasma, Bohm current from plasma sheath, and electron current from emission spots on the surfaces of mask and Pierce electrode, which are ignited at high voltage drops between the cathode plasma and the conducting surfaces. These three contributions are discussed in the following.

Within the allowable range of mask potentials the current of the ion beam does not depend on the mask potential. Thus, the contribution of the ion current to the mask current can be determined from the asymptotic behavior of the mask current for resistance $R_m \rightarrow \infty$, see Fig. 2.8.13, and is below 1 A. The same result is obtained by estimating the maximum possible ion currents from the target and grid plasmas. The ion current from the target plasma is bounded by complete neutralization of the electron beam:

$$\frac{J_i \beta c}{J_e v_i} \leq 1$$

For an electron current density of 3 A/cm² and a beam potential of ~30 kV against the target potential, we find $J_{imax} < 16$ mA/cm² or $I_{imax} < 0.5$ A. Similar values are obtained for the ion current from the grid plasma.

A strong indication for the formation of emission spots is an unstable operation of the accelerator. A continuous motion of the cathode spots, contraction and expansion, termination and re-ignition as observed in framing images strongly influence the cathode plasma parameters and result in an inhomogeneous emission behavior. An unstable regime is obtained for mask resistances below 300 Ohm.

For R_m values in the range of 300 to 2000 Ohm the mask current is determined predominantly by the saturation currents of ions and electrons in the plasma sheath:

$$I_m = I_i + I_e e^{-\frac{e\Delta\phi}{kT_e}}$$

Here I_i , I_e are the ion and electron saturation currents and $\Delta\phi$ is the potential drop between plasma and mask.

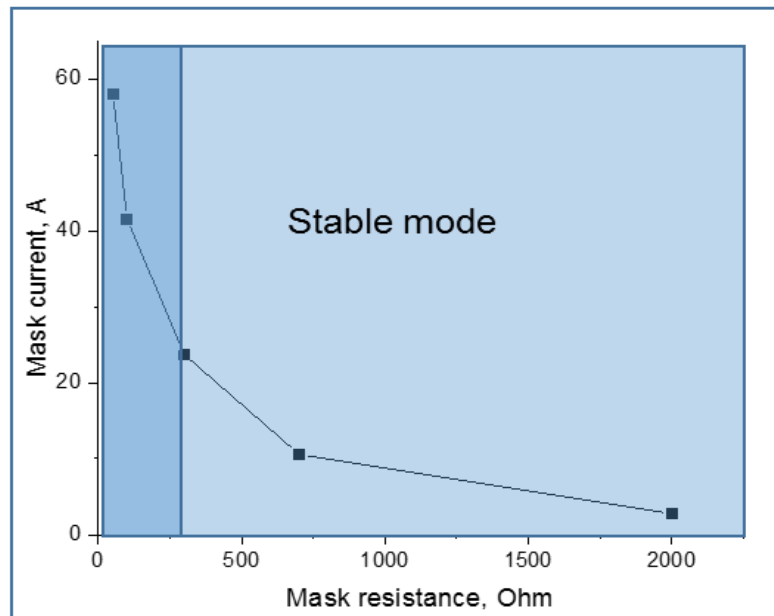


Fig. 2.8.13: Mask current versus resistance.

As long as the mechanism of current flow between plasma and mask does not change, the mask current is determined directly by the parameters of the cathode plasma and thus indirectly by the current through the carbon fiber tips, I_{tip} . Analysis of the current data shows that the ratio $\frac{I_m}{I_{tip}}$ remains almost constant during the pulse. This indicates stable plasma parameters. The evolution of $\frac{I_p}{I_m}$, however, shows a distinct rise after $\sim 30 \mu s$. This increase can be explained by an increase of the contact area between cathode plasma and Pierce electrode due to radial expansion of the plasma. Analysis of the ratio $\frac{I_g}{I_c}$ further confirms radial plasma motion perpendicular to the magnetic field lines. After $\sim 50 \mu s$ the grid current strongly increases at simultaneously decreasing emission current. This is only possible if the effective transparency of the grid decreases. With a radial extent of the cathode plasma exceeding the grid opening, more and more emitted electron strike the grid holder.

Although an increase of the magnetic field strength at the cathode does indeed result in a lower ratio of the grid current during the pulse (Fig. 2.8.14), the radial plasma expansion can not be avoided.

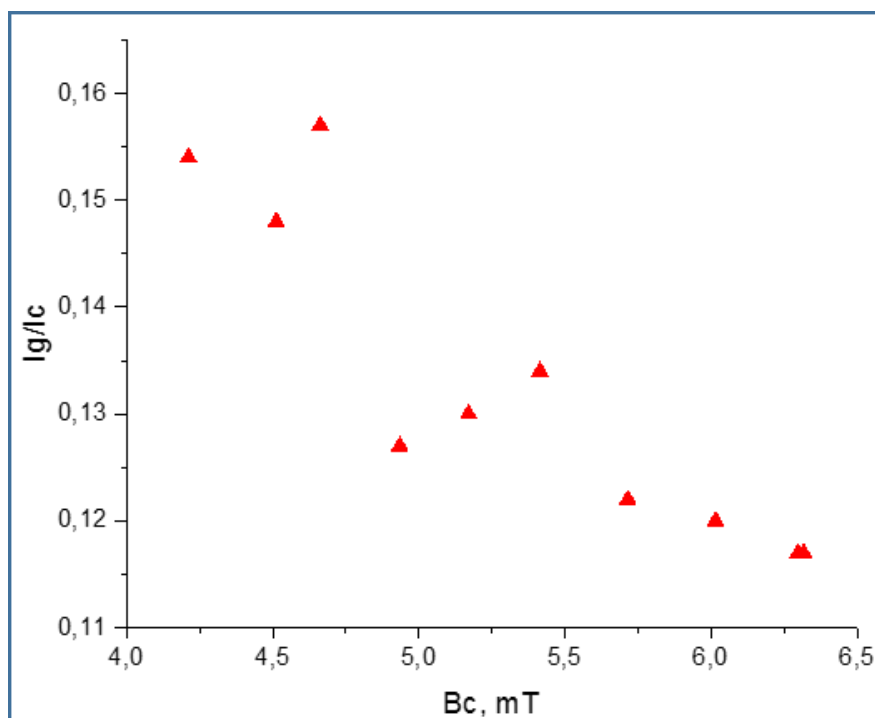


Fig. 2.8.14: Ratio of grid current versus magnetic field strength at cathode.

Results: Grid plasma

For default operation of GESA-SOFIE (mask current below 20 A), grid plasma is recognized after $\sim 45 \mu s$. Although light emission at the grid is observed very early in the pulse (Fig. 2.1.15), this does not necessarily indicate the existence of plasma. Plasma requires ionization rates in the vapor cloud exceeding recombination and ion emission towards the cathode. Once plasma is formed, it will expand towards the cathode. Therefore, expansion of the region showing light emission indicates the existence of plasma. After $\sim 45 \mu s$ the grid plasma starts to expand. At the same time the grid current increases. The fastest rise of I_g is observed for decreasing emission current. As discussed above, this is caused by the radial expansion of the plasma and the fact that an increasing number of emitted electrons strike the grid holder. The increase of the grid current leads to a decrease of the potential drop between cathode and grid. This results in a lower emission current.

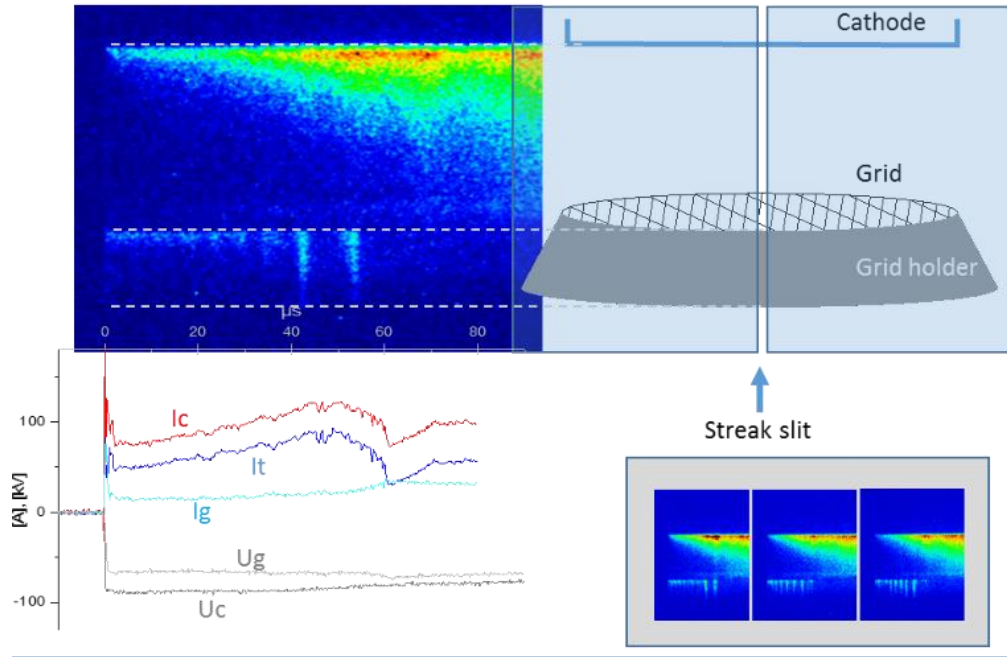


Fig. 2.8.15: Streak images of the cathode-grid region. The grid is imaged with a slight perspective deformation, the cathode without. The focus is on the front rim of the grid holder.

The cathode-grid voltage reaches a minimum after $\sim 60 \mu\text{s}$, then slightly increases and stabilized at $\sim 10 \text{ kV}$ for a rather long time (hundreds of μs). This stabilized potential drop depends on the plasma parameters. For high emission current a plasma with higher density is generated and the voltage drop is lowered to values around 3-4 kV. For thinner cathode plasmas, voltage drops of up to 13-14 kV were achieved.

The minimum of the voltage drop at $\sim 60 \mu\text{s}$ coincides with the minimum of the emission current and the maximum of the grid current. Obviously closure of the gap between the cathode plasma and the grid plasma occurs at that moment. Although the gap impedance reaches a minimum value, short-circuiting does not occur, because the current is limited by the saturation currents of the electrons,

$$J_e = en_k \sqrt{\frac{kT_{ek}}{2\pi m}} \text{ and ions, } J_i = en_g (0.4 \sqrt{\frac{kT_{eg}}{M}} + v_g).$$

Here, the indices "k" and "g" denote cathode and grid plasma and v_g is the expansion velocity of the grid plasma. Once this limit is reached, a double layer is formed across which the total voltage drop occurs. The further evolution of the double layer depends on the plasma parameters and the voltages applied by the circuit.

Plasma gap closure is hardly detectable by the streak images. The reason is that grid plasma is formed primarily adjacent to the grid holder and the location of the gap closure is expected to occur outside the transparent part of the grid. Due to the small extent of the grid plasma above the grid holder the optical path is not long enough to obtain a good signal.

Conclusion

The radial expansion of the cathode plasma significantly influences the operation of the accelerator. It induces processes that lead to a transition from a regime of vacuum between cathode and grid to a regime of plasma-filled cathode-grid gap. Whether this transition is advantageous or disadvantages for the application depends on the applicability of the electron beam formed in the double layer of the plasma-

filled regime. In any case, the reason of plasma expansion perpendicular to the magnetic field lines needs to be further explored in order to either suppress or control this process.

Another important aspect of future research is the control of the cathode plasma parameters. The aim is to uncouple the plasma generation rate and the perveance evolution of the system. Possible approaches are the introduction of a modified mask with larger contact area or the use of a plasma generator with independent power source.

Involved Staff:

DP W. An, A. Neukirch, Dr. A. Heinzl, DI (Fh) F. Lang, Prof. G. Müller, Dr. G. Schumacher (Gast), H. Shi (SCS-PhD student), A. Sivkovich, **Dr. A. Weisenburger**, W. Zhen (SCS-PhD student), DI (Fh) F. Zimmermann,